Impact of Crosstalk on Reflectivity and Doppler Measurements for the WIVERN Polarization Diversity Doppler Radar

Original
Impact of Crosstalk on Reflectivity and Doppler Measurements for the WIVERN Polarization Diversity Doppler Radar / Rizik, A., Battaglia, A., Tridon, F., Scarsi, F.E., Kötsche, A., Kalesse-Los, H., Maahn, M., Illingworth, A.. - In: IEEE TRANSACTIONS ON GEOSCIENCE AND REMOTE SENSING. - ISSN 1558-0644. - 61:(2023), pp. 1-14. [10.1109/TGRS.2023.3320287]

Availability:
This version is available at: 11583/2990107 since: 2024-07-01T15:00:03Z

Publisher:
IEEE

Published
DOI:10.1109/TGRS.2023.3320287

Impact of cross-talk on reflectivity and Doppler measurements for the WIVERN Polarization Diversity Doppler Radar

Ali Rizik, Alessandro Battaglia, Frederic Tridon, Filippo Emilio Scarsi, Anton Kötsche, Heike Kalesse-Los, Maximilian Maahn, and Anthony Illingworth

***Abstract*—The WIVERN (WInd VElocity Radar Nephoscope) mission, one of the four ESA Earth Explorer 11 candidate missions, aims at globally observing, for the first time, simultaneously vertical profiles of reflectivities and line of sight winds in cloudy and precipitating regions. WIVERN adopts a dual-polarization Doppler radar in order to overcome the short decorrelation time between successive radar pulses transmitted from low Earth-orbiting satellites with finite beamwidth antennas. WIVERN transmits a single polarization state at a time (H or V), receives in both polarization states, and uses the Polarization Diversity Pulse Pair (PDPP) technique to estimate the Doppler velocity. The weaker cross-polar signals can sometimes interfere with the co-polar ones, causing ghost signals in the measurements that hinder the system's overall performance. Additionally, with the envisaged radar trigger mode, parameters such as Linear Depolarization Ratio (LDR) and Differential Reflectivity (Z_{DR}) cannot be directly measured because of the nearly simultaneous transmission of H and V pulses. To overcome these challenges, this article presents a novel technique based on the Optimal Estimation (OE) algorithm for retrieving LDR, Z_{DR}, and co-polar reflectivity for radars operated in PDPP mode. The performance of the proposed method is evaluated using a realistic climatology of profiles simulated from CloudSat data. Results demonstrate that co-polar reflectivity can be accurately retrieved in regions with a good signal-to-noise ratio and in the absence of simultaneous cross-talk interference in both channels (which occurs very rarely). The LDR retrieval on the other hand is typically driven by the a-priori with a substantial impact of measurements only for the surface returns.**

The impact of cross-talk is also assessed on the reduction of precise Doppler measurements. Findings confirm that a selection of the separation between the two polarization diversity pulses (T_{HV}) of 20 μs achieves a good balance between the large errors originated by the strong dependence on the Doppler phase noise at small T_{HV}s and those caused by the drop in correlation and unambiguous Nyquist velocity at large T_{HV}.

***Index Terms*—Doppler radar, CloudSat radar, winds, polarization diversity, retrieval, co- and cross-polar signals, linear depolarization ratio, reflectivity differential ratio.**

A. Rizik, F. Tridon, and F. E. Scarsi are with the Department of Environment, Land and Infrastructure Engineering, Politecnico di Torino, Turin, Italy (e-mail: {ali.rizik, frederic.tridon, filippo.scarsi}@polito.it).

A. Battaglia is with the Department of Physics and Astronomy, University of Leicester, Leicester, UK; NCEO, Leicester, UK and DIATI, Politecnico di Torino, Turin, Italy (e-mail: ab474@leicester.ac.uk, alessandro.battaglia@polito.it).

A. Kötsche, H. Kalesse-Los, M. Maahn are with Leipzig Institute for Meteorology (LIM), Leipzig University, Leipzig, Germany (e-mail: {anton.koetsche, heike.kalesse, maximilian.maahn}@uni-leipzig.de).

A. Illingworth is with the Department of Meteorology, University of Reading, Reading, United Kingdom (e-mail: a.j.illingworth@reading.ac.uk).

Manuscript received Month DD, YYYY; revised Month DD, YYYY.

I. INTRODUCTION

THE WIVERN mission, currently undergoing Phase 0 studies within the ESA Earth Explorer 11 program, offers the prospect of acquiring in-cloud winds for the first time, thanks to a conically scanning Doppler radar ([1], [2]). To overcome the substantial uncertainties introduced by Doppler fading resulting from the satellite's fast motion, which reduces the decorrelation time between successive pulses and thereby diminishes the precision of Doppler velocity with classical pulse pair estimators [3], the mission proposes polarization diversity ([4], [5]). In addition to the innovative wind product, WIVERN has the potential to provide cloud products comparable to those of the CloudSat CPR [6] and planned for the EarthCARE CPR [7]–[9] but with an unprecedented revisit time, thanks to its rapid scanning rate (approximately 12 rpm) and slant viewing angle (approximately 42°). The sensitivity of the WIVERN system will be reduced compared to that of the CloudSat and EarthCARE CPR, with a nominal sensitivity at 5 km integration of -23 dBZ (compared to -34.5 dBZ and -28.5 dBZ for the EarthCARE and CloudSat CPR, respectively), due to its fast scanning. However, WIVERN observations will be impacted by contamination in the reflectivity signal caused by cross-polarization returns [1], [5], [10], leading to the production of returns in regions where no targets are present — known as "reflectivity ghosts" — or can positively bias reflectivities in presence of atmospheric targets. Cross-talk is normally caused by depolarization effects at backscattering [11] but can also be associated with multiple scattering [12], which is expected to be important for WIVERN mainly in deep clouds with large contents of dense ice particles [13].

While such ghosts will not bias the Doppler velocity measurements but will only decrease their precision [4], [10], it will be imperative to properly eliminate such reflectivity ghosts in order to obtain quantitative estimates of cloud and precipitation properties. This paper presents a technique based on optimal estimation for retrieving copolar and cross-polar reflectivities. The retrieval is applied to a climatology of WIVERN profiles reconstructed from CloudSat observations. This allows for assessing the impact of the cross-talk on WIVERN reflectivity measurements. Similarly, an analytical formula is used to quantify the deterioration of Doppler velocity precision caused by the ghosts. The dependence of the effects on the separation time between the two orthogonal polarization states is also thoroughly analyzed.

The approach is tailored to the WIVERN radar but it is applicable to all ground-based and airborne cloud radars adopting polarization diversity pulse pair to significantly increase the Nyquist velocity [4], [10], [14]. The paper is structured as follows: Sect. II briefly describes the pulse scheme that is used by polarization diversity pulse pair radars and presents a method to construct a climatology of realistic WIVERN profiles based on the CloudSat W-band radar observations. The optimal estimation technique for retrieving co-polar and cross-polar signals presented in Sect. III is applied to the CloudSat-based dataset. The impact of cross-talk between horizontal (H) polarized and vertical (V) polarized backscattered radiation both on the co-polar reflectivity retrieval and Doppler velocity estimates is discussed in Sect. IV with conclusions drawn in Sect. V.

II. THE POLARIZATION DIVERSITY PULSE PAIR (PDPP) TECHNIQUE

WIVERN employs the PDPP technique, utilizing alternating pulse pairs transmission between H-V (H-leading, V-trailing) and V-H (V-leading, H-trailing) pairs, as illustrated in Figure 1. Each pair of horizontally and vertically polarized pulses is separated by a very short interval, T_{HV}, (currently the optimal value selected for WIVERN is $20\,\mu$s, [2]) which guarantees a strong correlation between the two pulses, thus enabling the possibility of performing Doppler velocity estimates via pulse pair processing. On the other hand, the different pairs are transmitted with low PRF (of the order of 4 kHz with pulse repetition intervals of 250 μs) which allows for achieving unambiguous ranges of the order of 37.5 km, thus profiling the whole troposphere. This pulse scheme has the key advantage of solving the Doppler dilemma, i.e. decoupling the range ambiguity from the velocity aliasing and the phase decorrelation.

A. Definition of PDPP variables

Usually, H and V-pol pulses propagate and back-scatter independently; however, there may be sources of cross-talk between the two orthogonal polarizations. Assuming that the two transmitted pairs are sampling nearly the same volume (with two successive back-scattering volumes horizontally separated by a distance of 125 m, which is the footprint speed divided by the PRF), the received signals in the H and V receivers can be expressed as:

$$\text{H-V pair:} \quad \begin{cases} P_{\text{H}}^{\text{H-V}}[r] = P_{\text{HH}}[r] + P_{\text{VH}}[r - \Delta r_{T_{HV}}] \\ \qquad\qquad + N_{\text{H}}[r] \\ P_{\text{V}}^{\text{H-V}}[r] = P_{\text{VV}}[r] + P_{\text{HV}}[r + \Delta r_{T_{HV}}] \\ \qquad\qquad + N_{V}[r] \end{cases} \tag{1}$$

$$\text{V-H pair:} \quad \begin{cases} P_{\text{H}}^{\text{V-H}}[r] = P_{\text{HH}}[r] + P_{\text{VH}}[r + \Delta r_{T_{HV}}] \\ \qquad\qquad + N_{\text{H}}[r] \\ P_{\text{V}}^{\text{V-H}}[r] = P_{\text{VV}}[r] + P_{\text{HV}}[r - \Delta r_{T_{HV}}] \\ \qquad\qquad + N_{\text{V}}[r] \end{cases} \tag{2}$$

where $\Delta r_{T_{HV}} = cT_{HV}/2$ is the range associated with the time between the dual polarization pair, T_{HV}, N_{H} and N_{V} are the noise powers in the two receivers while the first and second subscript in the power terms P in the right-hand sides correspond to the transmitted and received polarization, respectively. All powers are intended expressed in linear units unless it is stated otherwise. An example of how the H and V-return echoes mix is shown in Fig. 1 for a scene including an ice cloud, a cloud-free region, and rain above a strongly reflecting surface. The returns in the leading pulse (H-pol) are plotted in blue and those in the trailing pulse (V-pol) (lagging by T_{HV}) in red. The dashed red line corresponds to the cross-talk associated with the leading pulse (and it is proportional to the back-scattered signal in the H-pol, but usually several dB lower in intensity). This signal is received in the V-channel and generates returns in regions that otherwise would appear void of hydro-meteors (hence the name ghosts). The grey-shaded areas represent ranges where the ghosts exceed the co-polar signal. The most pronounced ghost is the one produced by the strongly reflecting surface. With similar reasoning, the cross-talk generated by the V-pulse could be illustrated (not shown for clarity of purpose).

Note that, for spaceborne configurations (but not for airborne or ground-based applications when the range changes rapidly for the different hydrometeor targets in the troposphere), powers can be replaced by reflectivities because the ranges of all tropospheric targets are practically constant. The signal-to-noise ratios (SNR) are defined as:

$$\text{SNR}_{\text{H}}[r] \equiv \frac{P_{\text{HH}}[r]}{N_{\text{H}}[r]} \tag{3}$$

$$\text{SNR}_{\text{V}}[r] \equiv \frac{P_{\text{VV}}[r]}{N_{\text{V}}[r]} \tag{4}$$

It is also useful to introduce, for the H-V pair, the signal-to-ghost ratios (SGR) as:

$$\text{SGR}_{\text{H}}^{\text{H-V}}[r] \equiv \frac{P_{\text{HH}}[r]}{P_{\text{VH}}[r - \Delta r_{T_{HV}}]} \tag{5}$$

$$\text{SGR}_{\text{V}}^{\text{H-V}}[r] \equiv \frac{P_{\text{VV}}[r]}{P_{\text{HV}}[r + \Delta r_{T_{HV}}]} \tag{6}$$

with a similar definition for the V-H pair. An SGR=0 (-3) dB corresponds to a situation where the cloud signal is exactly equal to (half of) the ghost signal. In the following, other two quantities will be used:

$$\text{SGR}_{\text{min}}^{\text{H-V}}[r] = \min(\text{SGR}_{\text{H}}^{\text{H-V}}[r], \text{SGR}_{\text{V}}^{\text{H-V}}[r]) \tag{7}$$

$$\text{SGR}_{\text{max}}^{\text{H-V}}[r] = \max(\text{SGR}_{\text{H}}^{\text{H-V}}[r], \text{SGR}_{\text{V}}^{\text{H-V}}[r]) \tag{8}$$

The first is important when assessing the Doppler performance (the occurrence of low values of SGR_{min} implies a larger error in Doppler velocities), the latter the uncertainties in the retrieval of co-polar reflectivities.

Note that $Z_{\text{DR}} \equiv \frac{P_{\text{HH}}}{P_{\text{VV}}} = 0$ dB is assumed throughout the main part of this paper. This is supported by the fact that at the W-band for slant incidence angles close to 45°, the values of Z_{DR} of hydrometeors are close to 0 dB [15]. In this case, the co-polar signals for H and V polarization at each range r are identical and will be denoted by $P_{\text{co}}(r)$, i.e $P_{\text{HH}}(r) = P_{\text{VV}}(r) = P_{\text{co}}(r)$. Also $P_{\text{HV}}(r) = P_{\text{VH}}(r) = P_{\text{cx}}(r) = \text{LDR}(r) \times P_{\text{co}}(r)$ with LDR being the linear depolarization ratio (which is polarization-independent when

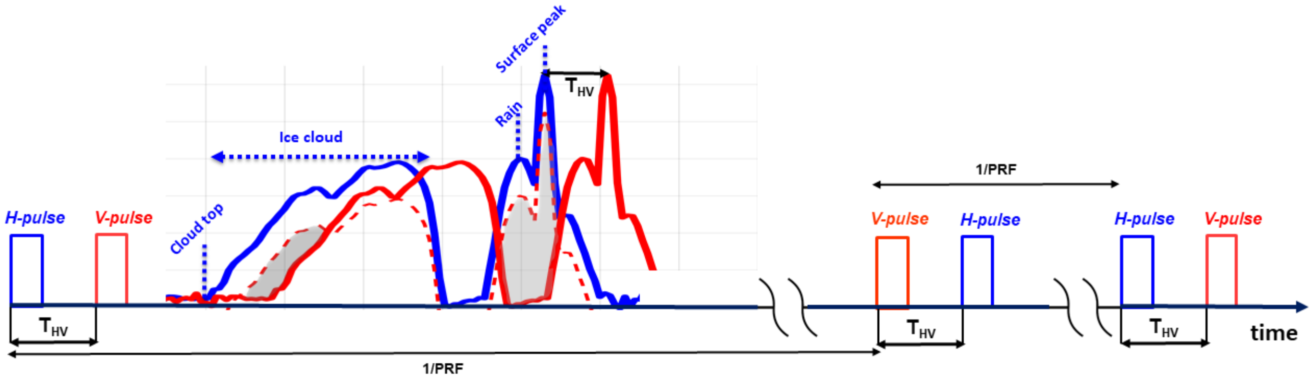

Fig. 1. Proposed pulse sequence for the WIVERN polarization diversity radar. Two pulses with different linear orthogonal polarizations (the terms H and V denote polarizations in the horizontal and vertical directions, respectively) are sent with a short pulse-pair interval, T_{HV}. The dashed line corresponds to the cross-talk of the leading pulse which interferes with the trailing pulse. The shaded regions correspond to ranges where in the V-receiver the cross-talk signal exceeds the co-polar signal (i.e. $\mathrm{SGR}_{\mathrm{V}}^{\mathrm{H\text{-}V}} < 0\,\mathrm{dB}$). The sequence is repeated with a much longer separation equal to the inverse of the Pair Repetition Frequency (PRF). The order of the polarization state of each pulse pair is switched from pair to pair in order to cancel out differential phase shift effects between the two channels. In this example, a sequence of three pairs is illustrated with two pairs (one pair) with H-(V-)pulse leading and V-(H-)pulse trailing.

$Z_{\mathrm{DR}} = 0\,\mathrm{dB}$, [16]). The most general case of Z_{DR} different from zero is treated in the Appendix for completeness.

B. Reconstruction of WIVERN profiles from CloudSat reflectivity observations

To evaluate the retrieval effectiveness in this scenario, realistic profiles simulated from CloudSat observations are utilized. The methodology, initially proposed by [17] and recently refined by [18], reconstructs W-band 42° slant-viewing profiles from nadir-looking profiles measured by the CloudSat CPR. This requires the introduction of a larger amount of attenuation because of the increase in the path through the attenuating atmosphere and the replacement of the surface clutter returns as a consequence of the dependence of the normalized backscattering cross section, σ_0, on the incidence angle [19]. Vertical profiles of linear depolarization ratios, LDR, are also constructed based on some climatological values associated with hydrometeor types and temperature (see [18]).

The co-polar H and V signals, along with their corresponding shifted cross-polar versions, are combined to create the WIVERN H and V signals by applying the formulas provided in Eq. 1-2, which involves shifting the cross-polar components by $\pm\Delta r_{T_{HV}}$. An example of the procedure is shown in Fig. 2. This profile is particularly interesting because it is characterized by strong vertical gradients of reflectivities and a highly depolarizing (land) surface. These two characteristics are the main sources of cross-talk. In fact, for the H-V pair, the WIVERN received signal in the H and V receivers is the result of combining the co-polar signal (red lines in the left panel) with the cross-polar signals shifted upward (magenta line) and downward (cyan line) for the V and the H receiver, respectively. The interplay between the vertical reflectivities and the strength of the cross-polar signals originates in regions where the cross-polar signals can become comparable with the co-polar signal itself. Such regions are highlighted by grey-shaded areas. Note that while in the upper (lower) shaded layer the cross-talk is present only in the V-channel (H-channel), the mid-layer cross-contamination occurs both in the H and in the V-channel. The latter situation is particularly tricky to handle.

TABLE I
BASELINE SPECIFICS CURRENTLY ENVISAGED FOR THE DUAL-POL DOPPLER RADAR OF THE WIVERN MISSION.

Spacecraft height, $H_{S/C}$	500 km
Spacecraft velocity, $v_{S/C}$	7600 ms^{-1}
Incidence angle, θ_i	41.6°
Radar frequency	94.05 GHz
Pulse length, τ	3.3 μs
Antenna beamwidth, θ_{3dB}	0.071°
Antenna angular velocity, Ω_a	12 rpm
Footprint speed due to conical scanning	500 kms^{-1}
Transmit polarization	H or V
Time separation between H and V pulses, T_{HV}	20 μs
Cross-polar isolation	<-25 dB
Single pulse sensitivity, $MDS_{0\,dB}$	-15 dBZ
H-V Pair Repetition Frequency, PRF	4 kHz
Number of H-V Pairs per 1 km horizontal distance integration	8

III. CO- AND CROSS-POLAR RETRIEVAL FROM WIVERN SIGNAL

Under the condition that $Z_{\mathrm{DR}}(r) = 0\,\mathrm{dB}$ for all ranges, all previous equations simplify based on the fact that $P_{\mathrm{VV}}(r) = P_{\mathrm{HH}}(r)$. Moreover, there will be only two unknowns at each range level, i, specifically $P_{\mathrm{co}}[i]$ and $P_{\mathrm{cx}}[i]$, for a total of $2N$ unknowns, N being the number of levels. In the case of a H-V pair such variables must be retrieved from Eq. (1) which provides a linear system of $2N$ equations in $2N$ unknowns. Likewise Eq. (2) will provide a solution for a V-H pair.

A. Iterative retrieval approach

An analytical retrieval method can invert such a linear system. To simplify the problem the profiles are digitized so that the distance $\Delta r_{T_{HV}}$ is an integer multiple of the range Δr, i.e. $\Delta r_{T_{HV}} = n_{HV}\Delta r$ (as depicted in Fig. 3). For instance, for the specifics of WIVERN (Tab. I) the sampling along the range is equal to 500 m ($\tau = 3.3\ \mu$s) whereas $\Delta r_{T_{HV}} = 3\,\mathrm{km}$ so that $n_{HV} = 6$.

While neglecting the noise at this point, the measurements at level i are solely influenced by the reflected powers at level

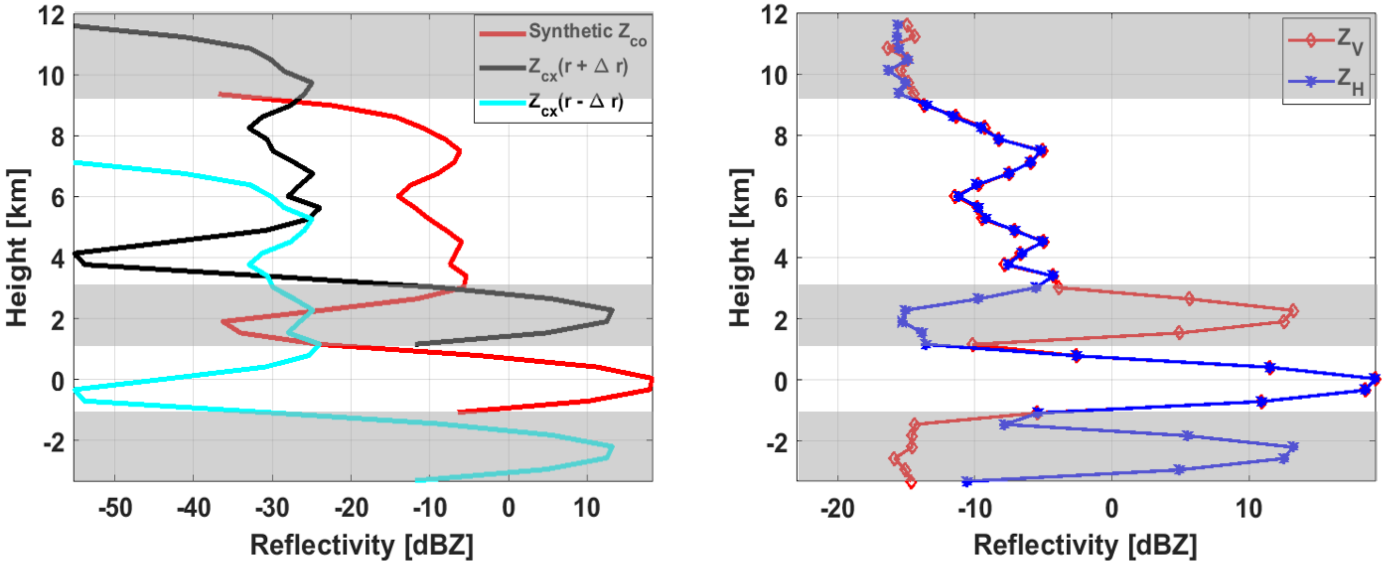

Fig. 2. Example of simulated WIVERN H and V signals inclusive of noise (right panel) derived from a CloudSat profile (left panel). In the left panel, the red line represents the synthetic CloudSat co-polar profiles whereas the black and the cyan lines correspond to the cross-polar signal derived by multiplying the co-polar signal for climatological LDR profiles and by shifting it by $\pm\Delta r_{20\,\mu s} = 3$ km, i.e. a shift $\pm\Delta z_{20\,\mu s} = 2.24$ km in height. Areas affected by $\text{SGR}_{\text{min}} < 0$ (i.e. at least one of the cross-talk signals exceeds the co-polar signal) are highlighted by grey shading.

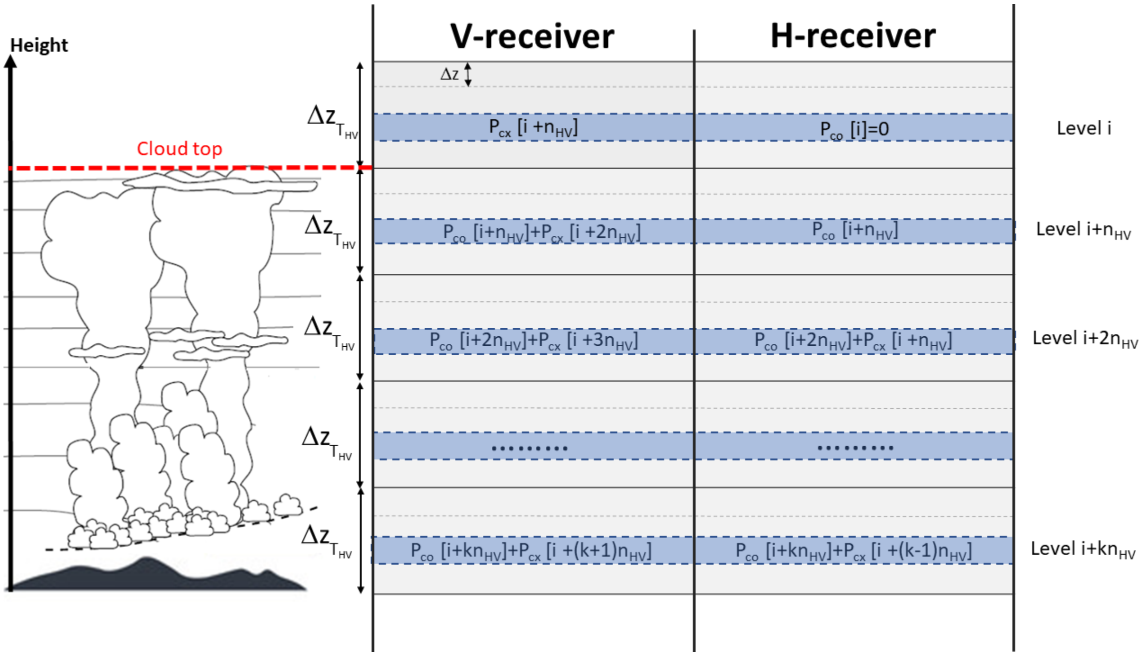

Fig. 3. WIVERN H and V reflectivity profiles separated into different layers separated by $\Delta r_{T_{HV}}$ in range and by $\Delta z_{T_{HV}}$ in height. Each layer has n_{HV} levels (here only four just for illustrative purposes). The subscripts co and cx indicate co-polar and cross-polar signals, respectively. Here H is the leading pulse.

$i-n_{HV}$, i, and $i+n_{HV}$. Therefore, only the layers highlighted in blue in Fig. 3 are correlated with each other. Solving the system (1) through iterative methods is straightforward. For instance, by subtracting in the system (Eq. 1) the first equation expressed at the i level from the second equation expressed at the $i-2n_{HV}$ level (i.e., Eq. 9):

$$P_{\text{V}}^{\text{H-V}}[i-2n_{HV}] = P_{\text{co}}[i-2n_{HV}] + P_{\text{cx}}[i-n_{HV}] \tag{9}$$

It is found that the iterative solution for the co-polar and cross-polar signal is:

$$\begin{cases} P_{\text{co}}[i] = P_{\text{H}}^{\text{H-V}}[i] - P_{\text{V}}^{\text{H-V}}[i-2n_{HV}] \\ \qquad + P_{\text{co}}[i-2n_{HV}] \\ P_{\text{cx}}[i] = P_{\text{V}}^{\text{H-V}}[i-n_{HV}] - P_{\text{H}}^{\text{H-V}}[i-n_{HV}] \\ \qquad + P_{\text{cx}}[i-2n_{HV}] \end{cases} \tag{10}$$

which can be properly initialized at the top of the cloud as in Fig. 3. This allows finding all co-polar and cross-polar powers for the layers identified in blue in Fig. 3. The same iterative procedure can then be repeated for $\forall i = 1, 2, \ldots, n_{HV}$. In the absence of noise, the set of Eqs. 10 can perfectly recover the co-polar and cross-polar powers using the V- and H-receiver powers.

B. Optimal estimation framework

When noise is present (i.e. when N_{V} and N_{H} cannot be neglected in Eq. 1), Eq. 10 does not provide an exact solution anymore, particularly at low SNRs. Other inversion techniques, such as Optimal Estimation (OE) [20], need to be adopted. The optimal estimation algorithm is an iterative process used to estimate unknown parameters of a system, given measurements with known errors, some prior knowledge of the unknowns, and a forward model of the measurements from the set of unknowns.

Specifically, for $Z_{\text{DR}} = 0$, the OE method is used to retrieve the co-polar power and LDR $\equiv P_{\text{cx}}/P_{\text{co}}$. The OE building blocks are as follows.

1) Unknowns:
The atmospheric properties $P_{\text{co}}[j] \equiv P_{\text{co}}(r_j)$ and LDR$[j] \equiv$ LDR(r_j) are retrieved for every range r_j, extending from the cloud top down to 1.5 km below the surface level, with a range resolution of 500 m. To identify the cloud top, a noise-subtracted version of Z_{V} and Z_{H} are first considered. The cloud top is identified by the height below which both Z_{V} and Z_{H} are consistently 1.0 dB greater than the radar sensitivity:

$$[\min(Z_e)]_L \equiv MDS_{0\,\text{dB}} - 5\,\log_{10} N_{\text{samples}} \tag{11}$$

where $MDS_{0\,\text{dB}}$ is the WIVERN single pulse sensitivity ($MDS_{0\,\text{dB}}$ = -15 dBZ), and the term on the right-hand side of Eq. (11) accounts for the increase in sensitivity associated to averaging independent samples, N_{samples}, over an integration length L (e.g. 40 for 5 km integration, given that one pair H-V is transmitted every 125 m), which is proportional to $\sqrt{N_{\text{samples}}}$.

2) Measurements:
$P_{\text{H}}^{\text{H-V}}[j]$ and $P_{\text{V}}^{\text{H-V}}[j]$ sampled with the same resolution as the unknowns but on a range which is extended by $\Delta r_{T_{\text{HV}}}$ above cloud top and below the lowest level below the surface. The uncertainty on the total power (noise plus signal) measurements (expressed in logarithmic units) is defined as:

$$\sigma_{Z_{\text{H,V}}}[\text{dB}] = \frac{4.343}{\sqrt{N_{\text{samples}}}}. \tag{12}$$

3) Forward Model:

$$P_{\text{H}}^{\text{H-V}}[i] \quad = P_{\text{co}}[i] + \text{LDR}[i - n_{HV}]\; P_{\text{co}}[i - n_{HV}]$$

with LDR expressed in linear units.

4) Methodology for choosing the a-priori:
   a) First, estimate P_{co} using the iterative approach. Then put all the P_{co} values that are less than a predetermined threshold to Not a Numbers (NaNs), which is chosen to be at least 1 dB higher than the WIVERN single pulse sensitivity ($thresh = MDS_{0\,\text{dB}} + 1$). Next, determine the minimum value among the iterative solution, P_{H}, and P_{V}. Then, subtract the noise from the resulting vector and replace the negative powers with NaNs. Finally, determine all the indices with negative powers and NaNs, and replace them with the radar sensitivity value in Eq. (11).
   The uncertainty on the co-polar a-priori is set to ± 5 dB in regions where SNR $\leq MDS_{0\,\text{dB}}$ and ± 3 dB everywhere else.
   b) Next, estimate P_{cx} using the iterative method. Then, subtract the noise from the resulting vector and replace any negative values with NaNs. With the resulting P_{cx} vector and the a-priori of P_{co}, calculate the LDR. Finally, put to NaNs all LDRs corresponding to ranges where:

$$\text{SNR(r)} \leq \begin{cases} 3\text{ dB for the surface} \\ 12\text{ dB for the atmosphere} \end{cases} \tag{13}$$

   c) Compute $\text{SGR}_{\text{H}}^{\text{H-V}}$ and $\text{SGR}_{\text{V}}^{\text{H-V}}$ using the previously computed P_{cx}, and P_{co}
   d) Define ranges r where, possibly, the iteration method provides a good a-priori for LDR, i.e. where:

$$\begin{aligned} &\min[\text{SGR}_{\text{H}}^{\text{H-V}}(r + \Delta r_{T_{HV}}), \\ &\text{SGR}_{\text{V}}^{\text{H-V}}(r - \Delta r_{T_{HV}})] \leq 3\text{ dB} \end{aligned} \tag{14}$$

   e) Fill in these ranges with LDR estimated from (a) and replace all other ranges with climatological hydrometeor LDR based on temperature as [18]:

$$\text{LDR}_{\text{a}} = \begin{cases} -20\,\text{dB}, & T < -3^\circ \\ -16\,\text{dB}, & -3^\circ \leq T \leq 3^\circ \\ -25\,\text{dB}, & T > 3^\circ \end{cases} \tag{15}$$

   The uncertainties on LDR a-priori are also defined based on temperature as follows:

$$\sigma_{\text{LDR}_{\text{a}}} = \begin{cases} 5\,\text{dB}, & T < -3^\circ \\ 3\,\text{dB}, & -3^\circ \leq T \leq 3^\circ \\ 3\,\text{dB}, & T > 3^\circ \end{cases} \tag{16}$$

   in order to capture that there is more uncertainty in the ice LDR as observed in the measurements taken at the Chilbolton observatory ([18]). The simulation of the LDR profiles used in this study is further illustrated in appendix B4.

5) OE iterative process: the differences between the predicted and actual measurements, known as the residuals, are used to update the unknown estimates according to [20]:

$$\begin{aligned} X_{i+1} = X_i + (K_i^T S_\epsilon K_i + S_a^{-1})^{-1} \\ (K_i^T S_\epsilon (Y - F(X_i)) + S_a^{-1}(X_a - X_i)) \end{aligned} \tag{17}$$

where X_i is the optimal solution obtained at each iteration i, X_a is the prior guess of the unknowns, S_a is the prior covariance matrix, S_ϵ is the measurement noise covariance matrix, $K_i = K(X_i)$ is the Jacobian matrix, Y is the measurement vector, and F is the

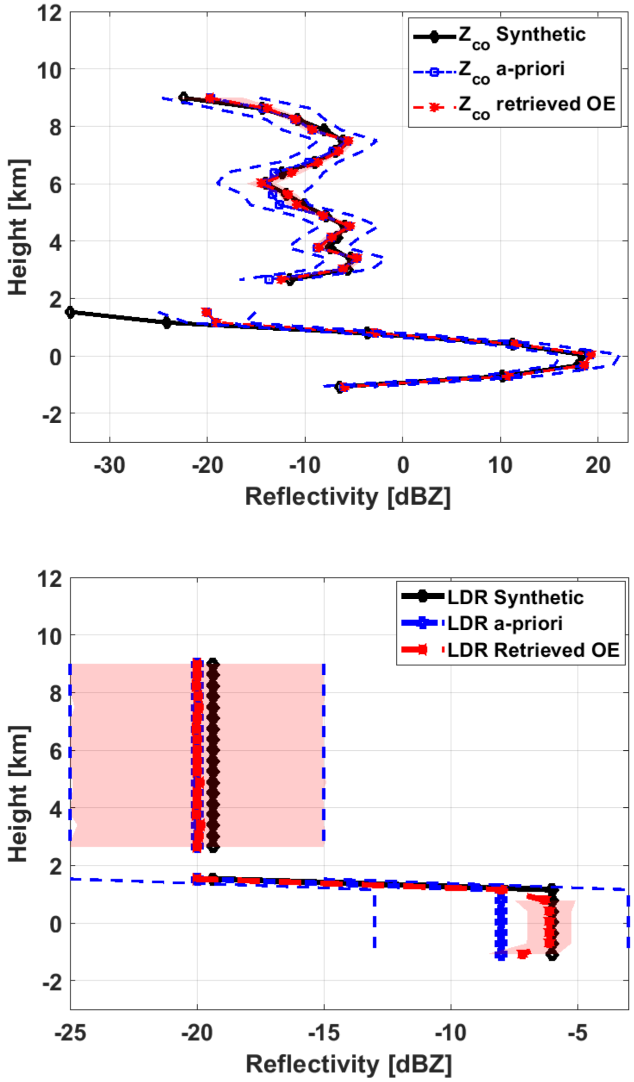

Fig. 4. Retrieved co-polar reflectivity (top) and LDR (bottom) for the profile shown in Fig. 2. A-priori and synthetic profiles are shown in blue and black color. A 5 km horizontal averaging is considered. The error standard deviation of the OE solution is shaded in red while the blue dashed lines represent the uncertainty on the a-priori.

forward model. The iterative procedure terminates when the convergence parameter

$$C_i \equiv (X_i - X_{i+1})^T \hat{S}^{-1}(X_i - X_{i+1}) \qquad (18)$$

where

$$\hat{S} = (S_a^{-1} + K_i^T S_\epsilon K_i)^{-1} \qquad (19)$$

is much less than n, the number of unknowns, (i.e., $C_i < \min(1, \frac{n}{10})$).

6) Finally, intervals exhibiting co-polar reflectivity retrievals that fail to surpass the radar sensitivity by a minimum of 1 dB are eliminated, i.e. no cloud is detected by WIVERN at such ranges.

C. Example of retrieved profile

The profiles of Z_{co} and LDR retrieved for the signal profile shown in Fig. 2 are presented in Fig. 4. Our findings demonstrate that the proposed co-polar a-priori approach produces an excellent fit for the co-polar reflectivity in areas with favorable SNR. However, as the SNR decreases, the co-polar a-priori profiles become unreliable. For heights between 0.8 and 2.6 km, the retrieved reflectivities are below the detection limit; therefore, no Z_{co} estimate is actually produced.

On the other hand, retrieving LDR is much more challenging. The retrieved LDR does not deviate much from the prior profiles apart for ranges corresponding to the surface return, which are the ranges that, via large cross-talk, produce SGR values lower than 0 above and below the surface peak (grey bands in Fig. 2) and large SNR. Only in such conditions do the measured Z_{H} and Z_{V} signals carry some information about LDR that the optimal estimation can extract.

It is worth highlighting that the red shading on the uncertainty of the errors from the optimal estimation is very small for the retrieved co-polar (top plot of Fig. 4) which makes it difficult to be noticed.

IV. APPLICATION TO THE CLOUDSAT-DERIVED DATASET

The performances of our retrievals have been tested on a one-month dataset of WIVERN profiles produced from CloudSat data based on the technique proposed by [18]. The dataset provides a robust climatology of realistic profiles that could be sampled by a WIVERN radar operated in a polar sun-synchronous orbit. The dataset combines CloudSat 94 GHz reflectivity observations, ECMWF winds, and climatological values of LDR (collected at the Chilbolton observatory, [18]) to produce slanted profiles of co- and cross-polar reflectivities in the WIVERN slant observation geometry. Such profiles are then combined as in Eqs. (1-2) with the noise level appropriate to the WIVERN system to produce WIVERN observables (Z_{H} and Z_{V}).

A. Results on Cloudsat data

An example of a snow precipitating system observed by CloudSat on the 18th of January 2007 over land (Fig. 5) is used to demonstrate our retrieval procedure. All clouds are at subfreezing temperatures. The true fields of Z_{co} and LDR are shown in the top panels. The precipitating system is over land which is characterized by a strong return and a strong LDR. The simulated WIVERN observations (inclusive of noise at $MDS_{0\,\text{dB}}$) clearly show the presence of ghosts generated by the strong surface cross-talk with enhanced reflectivity signal in correspondence to $\pm\Delta z_{T_{HV}} \approx 2.2$ km, where $\Delta z_{T_{HV}} = \Delta r_{T_{HV}} \times \cos[\theta_i]$ (Tab. I). The retrieved variables (fourth row) show excellent performances for Z_{co} (with a very effective subtraction of the ghosts) whereas it is clear that the LDR is mainly driven by the prior information, apart from ranges corresponding to the surface where the presence of the surface-generated ghosts allows a comprehensive reconstruction of the surface LDR as well. Errors in the co-polar reflectivities are generally lower than 1 dB with increased noisiness typically seen only in regions of low SNR. Errors in LDR are mainly mirroring prior errors, with smaller uncertainties in correspondence to the surface, which is the only place where the measurements are impacting the LDR retrieval.

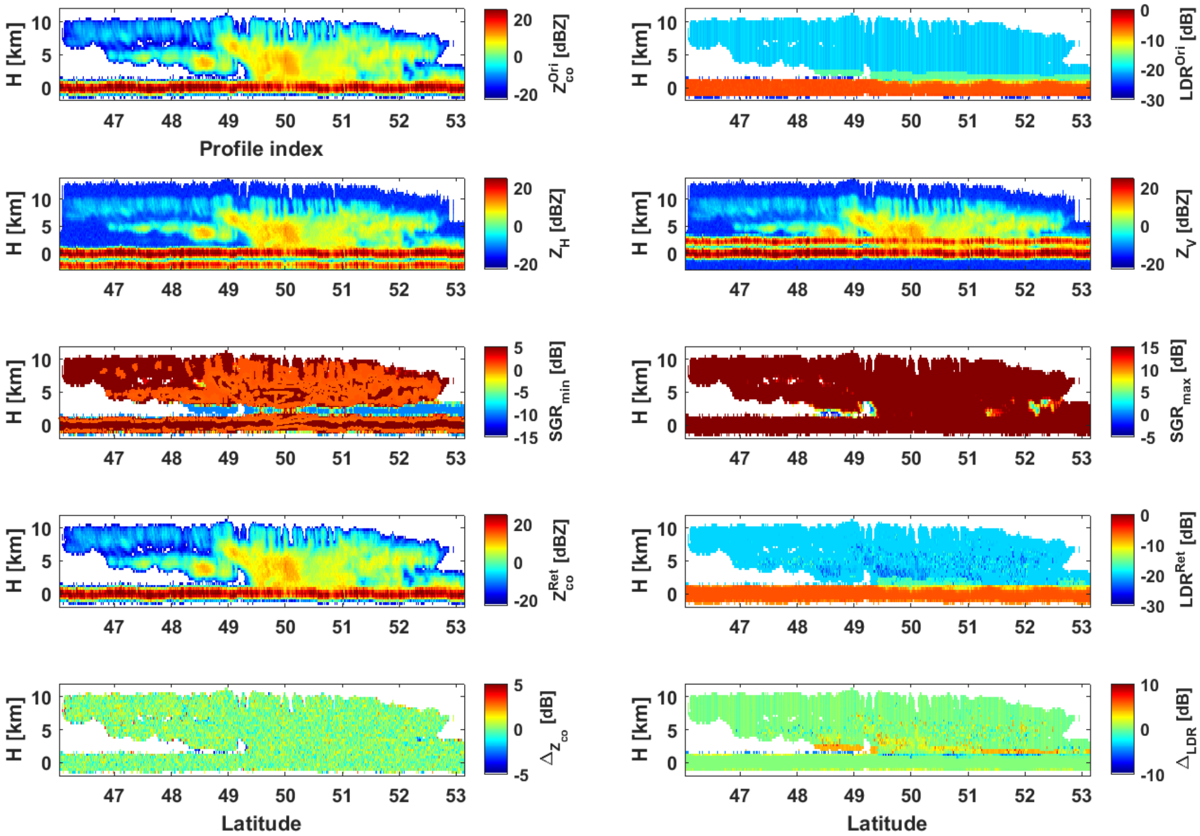

Fig. 5. Performance of the retrieval on a scene extracted from the CloudSat orbit: 2007-018-230022-03868. Top-row panels: true co-polar reflectivity and LDR; second-row panels: received leading pulse and trailing pulse reflectivity; third-row panels: SGR_{min} with the contour of the std of Doppler Line of Sight (LOS) winds in the left column, and SGR_{max} in the right one; fourth-row panels: retrieved co-polar reflectivity and LDR; last row panels: errors in the retrieved co-polar reflectivity and LDR (the difference between the original and the retrieved).

B. Statistical analysis

It is important to establish what is the impact of cross-talk in WIVERN measurements and, more specifically, how frequently the ghosts impact the reflectivity and the Doppler measurements. WIVERN profiles simulated based on one year (2007) of CloudSat data according to the procedure previously described have been used to estimate the frequency of “single” and “double” ghosts, i.e. of ranges at which the cross-talk is contaminating the signal of at least one or both the leading and trailing pulse, respectively. In the latter case, the previous retrieval examples suggest that recovering the co-polar reflectivity will be troublesome; in the former case additional noisiness (but no bias) is expected in the Doppler estimates [2], [4]. This is because being generated at a different backscattering volume, the cross-talk is incoherent with the co-polar signal.

Fig. 6 shows the absolute frequency (normalized to the total number of copolar reflectivities exceeding -20 dBZ) of occurrences of “single” (bottom) and “double” (top) ghosts for $T_{HV} = 20\,\mu$s.

1) Impact of cross-talk on reflectivities: double ghosts are present in correspondence of low SGR_{max} values. From the top panel of Fig. 6 such values are clustered at low Z_{co} values (certainly lower than 0 dBZ), with their probability of occurrence increasing more and more with lower and lower reflectivities. For instance for $-10 \leq Z_{co} \leq -9$ dBZ ($-20 \leq Z_{co} \leq -19$ dBZ) only 0.006% (0.027%) of the profile have SGR_{max} lower than 3 dB. Overall the presence of very strong double ghosts (i.e. with $SGR_{max} < -6$ dB) is very unlikely, i.e. 0.019% of the total (see results in Tab. II). This percentage decreases substantially when moving to shorter T_{HV} because the cross-talk associated with the surface (the main source of low SGR_{max} values) ends up in the first 2 km, which is excluded from the analysis because of clutter contamination. The same drop in the frequency of double ghost occurs when considering $T_{HV} = 40\,\mu$s. In this case, only in very deep systems (thicker than 8.8 km) double ghosts are physically possible, which excludes most of the cases.

To evaluate the efficacy of the retrieval technique, a statistical analysis of the errors in the retrieved co-polar reflectivities is conducted. The co-polar error is defined as the difference

TABLE II

FREQUENCY OF OCCURRENCE (IN %) OF "SINGLE" AND "DOUBLE" GHOSTS WITH DIFFERENT THRESHOLDS OF SGR_{MIN} AND SGR_{MAX}, RESPECTIVELY WITH DIFFERENT VALUES OF T_{HV}.

	$\text{SGR}_{\min}$	< -6	< -3	< 0	< 3	< 6
f [%]	10 μs	4.8	6	7.6	10.3	14.6
	20 μs	10.9	12.74	15.3	18.8	23.5
	40 μs	9.82	11.53	13.7	16.3	19.16

	$\text{SGR}_{\max}$	< -6	< -3	< 0	< 3	< 6
f [%]	10 μs	0.004	0.013	0.036	0.09	0.2
	20 μs	0.019	0.04	0.09	0.19	0.35
	40 μs	0.007	0.015	0.034	0.05	0.08

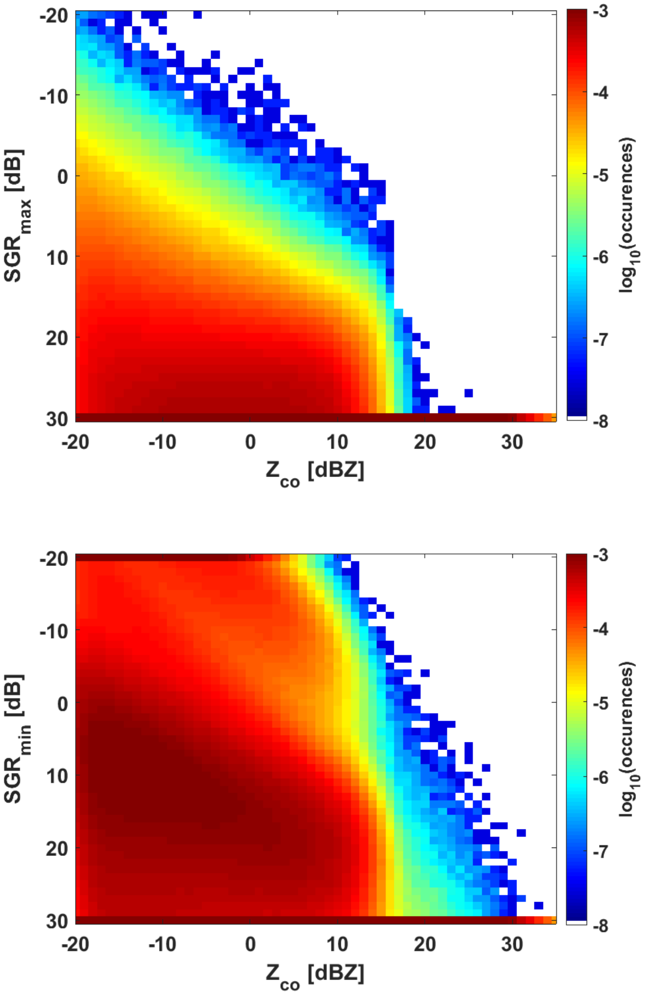

Fig. 6. Absolute frequency of the occurrences of "single" (bottom) and "double" (top) ghosts (with a given strength identified by the SGR value, y-axis) as a function of the co-polar reflectivity, x-axis for $T_{HV} = 20\ \mu$s. The binning size is 1 dB for both Z_{co} and SGR. In the first and last rows, all values exceeding the highest or being lower than the lowest SGR range of values are summed up together.

between the actual co-polar reflectivity and the retrieved co-polar reflectivity (e.g. see the bottom left panel in Fig. 5). Higher co-polar retrieval errors are expected in regions of low SNRs and with decreasing values of SGRs.

In order to understand how "double ghosts" adversely affect the Z_{co} retrieval, errors of such variables have been clustered according to different classes of SNRs and SGRs for any height above 2 km for a whole month of CloudSat data. Fig. 7 presents the mean and standard deviation of the Z_{co} retrieval errors as a function of the SNR for two different classes of $\text{SGR}_{\max}$, as indicated in the legend. As expected, with very large SGR there is no impact of the ghosts, the retrieval quality improves with SNR and the reflectivity errors saturate near 0.7 dB at high SNR, which corresponds to the theoretical value of $\frac{4.343}{\sqrt{N_{\text{samples}}}}$ with $N_{\text{samples}} = 40$. The error tends to increase at lower SNR becoming twice as large at SNR=0 dB, in line with theoretical expectations. In contrast, in the presence of SGR values between 0 and 5 dB, errors tend to be generally higher across all SNR and they tend to saturate at similar values as when no ghosts are present only at high SNR.

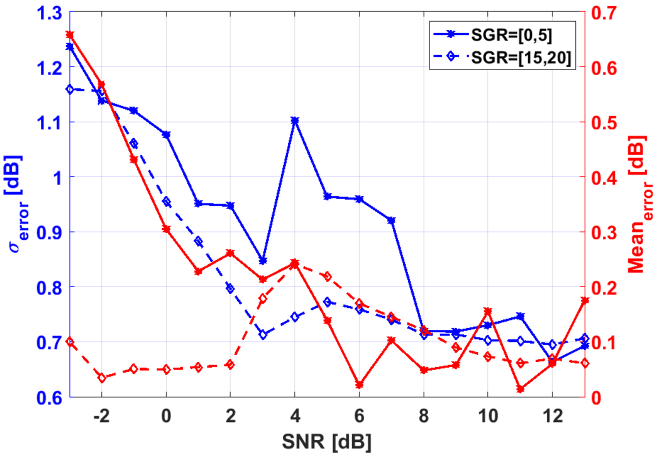

Fig. 7. Mean and standard deviation of the histograms of ΔZ_{co} as a function of SNR measured at a particular height between 5 and 8 km.

2) *Impact of cross-talk on Doppler velocities:* the impact of cross-talk on the Doppler velocity estimates can be estimated by considering the pulse pair estimator errors as the main drivers of the Doppler velocity error budget and by neglecting other errors related to mispointing, non-uniform beam filling, and wind shear [2]. The pulse-pair estimator Doppler velocity error can be approximated by the formula [2], [4]:

$$\sigma_{\hat{v}_D} = \frac{v_{\max}}{\pi\beta\sqrt{2N_{\text{samples}}}}\left[\left(1+\frac{1}{\text{SNR}}\right)^2+\frac{1}{\text{SGR}_\text{V}\text{SGR}_\text{H}}+\left(1+\frac{1}{\text{SNR}}\right)\left(\frac{1}{\text{SGR}_\text{V}}+\frac{1}{\text{SGR}_\text{H}}\right)-\beta^2\right]^{\frac{1}{2}} \qquad (20)$$

where the Nyquist velocity is equal to

$$v_{\max} \equiv \frac{\lambda}{4\,T_{HV}}$$

and the correlation between the H and V pulses is:

$$\beta \equiv \rho_{HV}(0)\, f_{vol}(T_{HV}) \exp\left(-\frac{8\pi^2\sigma_D^2\,T_{HV}^2}{\lambda^2}\right)$$

with $\rho_{HV}(0)$ the co-polarized correlation coefficient at lag-0 (see Appendix B for expected values), λ the radar wavelength and σ_D the Doppler spectral width. $f_{vol}(T_{HV})$ is the fraction of overlapping backscattering volumes between successive pulses due to the antenna rotation, which varies linearly from 1 at $T_{HV} = 0\ \mu$s to 0.944 at $T_{HV} = 60\ \mu$s (not shown). In the case of $\mathrm{SGR_{max}}$ significantly larger than 0 dB, the formula further simplifies and it is basically driven by the $\mathrm{SGR_{min}}$ value only. In such approximation Fig. 8 shows the impact of different values of SGR onto the standard deviation of the Doppler velocity estimates when considering a $T_{HV} = 20\,\mu$s and 5 km horizontal integration. At high SNRs an $\mathrm{SGR_{min}} = 0$ dB (-5) produces an error 4.0 (6.9) times bigger than in the absence of ghosts. Note also that Eq. (20) tends to slightly underestimate the error at low SNRs (dashed lines vs continuous lines which corresponds to Monte Carlo I&Q simulations).

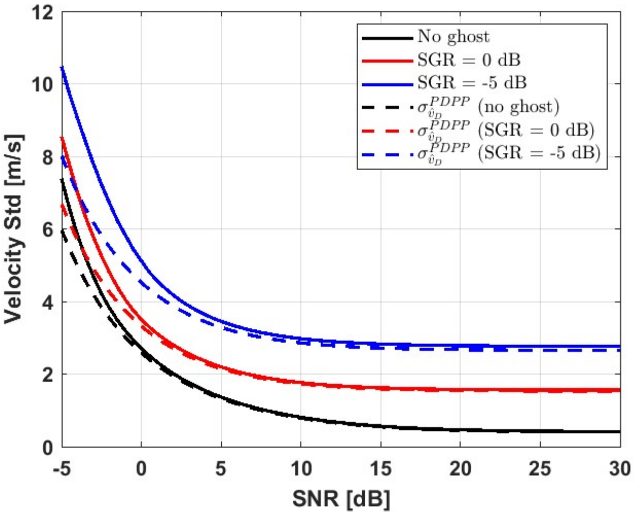

Fig. 8. Doppler velocity uncertainties as a function SNR for different SGRs at $T_{HV} = 20\,\mu$s. $\sigma_{\mathrm{D}} = 2.5$ m/s has been assumed. Results have been obtained with Monte Carlo simulations (continuous lines) and with the approximate formula (20) (dashed lines).

A general assessment of the impact of the ghosts on the Doppler estimates of the line of sight winds can be performed by applying Eq. (20) to the SNR and SGR values derived from the simulated WIVERN profiles from the CloudSat database. The investigation encompassed varying values of T_{HV} (which is known to affect the position of the ghosts and the errors in the pulse pair estimator, [4], [5]) and different strength of the cross-talk levels (by changing the LDR levels from the climatological reference). Fig. 9 clearly demonstrates that higher values of T_{HV} correspond to a greater number of precise wind with $T_{HV} = 40\ \mu s$ yielding 3.7 and 1.4 times more precise winds than 10 and 20 μs, respectively (see also Tab. III). Note how the profiles for the different T_{HV}s show all a dip in the number of profiles in correspondence to the heights (equal to $cT_{HV}\cos\theta_i/2$) at which ghosts generated by the surface appear in the trailing pulse. Conversely, the impact of LDR enhancement (i.e., the amplification of the ghost signal by a factor corresponding to the enhancement in LDR) on wind precision is noteworthy, particularly at lower T_{HV} values ($T_{HV} \leq 10\ \mu$s), where a 10 dB LDR enhancement resulted in a significant decrease in the number of precise winds (compare first three rows in Tab. III). However, this decrease becomes progressively less significant at higher T_{HV} values, ultimately becoming almost negligible at $T_{HV} = 40\ \mu$s (last three rows in Tab. III), thereby indicating reduced sensitivity to LDR enhancement. These results seem to suggest that $T_{HV} = 40\,\mu$s is the most favorable choice for the WIVERN radar. However, there is a clear drawback of larger T_{HV}s, that is the lower Nyquist velocities (e.g. 20 m/s for $T_{HV} = 40\,\mu$s). When dealing with $T_{HV} \leq 50\ \mu$s dealiasing with winds should not be a challenging task because of the larger Nyquist intervals, usually much bigger than typical uncertainties in winds from global models. On the other hand, there will be an issue associated with the bias in the velocity estimates when measuring winds in the proximity of the Nyquist (or folding velocities) velocity [21].

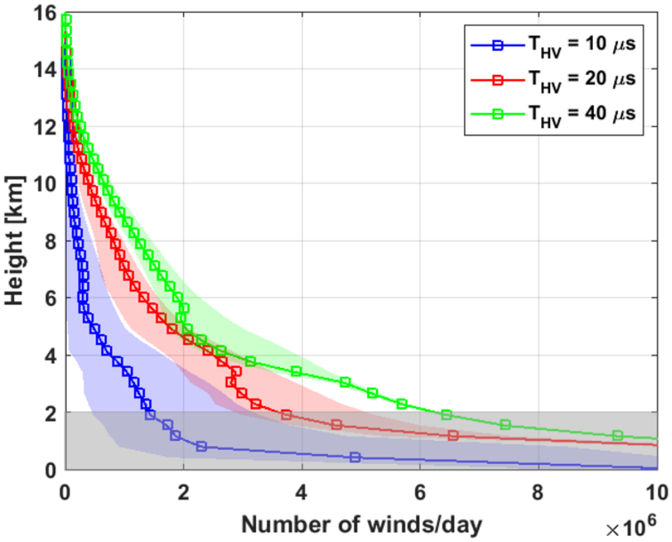

Fig. 9. Profile of number of 5-km averaged winds better than 1 m/s for different T_{HV} under distinct ghost signal scenarios. The continuous lines indicate the case with normal LDR condition, while the shading spans each line from the 10 dB LDR enhancement and the no-ghost condition. The grey shading corresponds to the ground clutter.

Fig. 10 depicts the expected probability distribution function on the observed Line of Sight (LOS) winds for azimuthal angles between 0° and 180° (winds of the opposite sign will be observed for azimuthal angles between 180° and 360°), as derived from the CloudSat+ECMWF synthetic dataset. Since Doppler spectra widths are expected of the order of $\sigma_{\mathrm{D}} = 2.5$ m/s the regions within $\pm\sigma_{\mathrm{D}}$ across the folding velocities (color-coded according to three different T_{HV} selections) are prone to velocity biases. Clearly, the highest value of T_{HV}, 40 μs, (the lowest value of T_{HV}, 10 μs) here considered has the highest fraction, 9%, (lowest fraction, 0.01%,) of potentially biased winds.

V. CONCLUSION AND FUTURE WORK

The WIVERN (WInd VElocity Radar Nephoscope) mission, one of the four ESA Earth Explorer program candidate missions, aims at globally observing, for the first time, vertical profiles of reflectivities and line of sight winds in cloudy and precipitating regions. In this work, the impact of cross-talk between horizontal (H) polarized and vertical (V) polarized backscattered radiation of the polarization diversity WIVERN W-band Doppler radar system has been investigated.

TABLE III
COMPARISON BETWEEN THE NUMBER OF DETECTED WINDS PER DAY BY THE WIVERN SYSTEM FOR DIFFERENT VALUES OF T_{HV} AND AT DIFFERENT LDR CONDITIONS FOR A PRECISION OF 1 M/S AT 5 KM HORIZONTAL INTEGRATION LENGTH.

T_{HV}	LDR condition	Number of winds/day [millions]
10 μs	No LDR	11.6
	LDR with no enhancement	5.7
	10 dB LDR enhancement	2.7
20 μs	No LDR	17.9
	LDR with no enhancement	15.9
	10 dB LDR enhancement	13.5
40 μs	No LDR	22.6
	LDR with no enhancement	21.1
	10 dB LDR enhancement	20.1

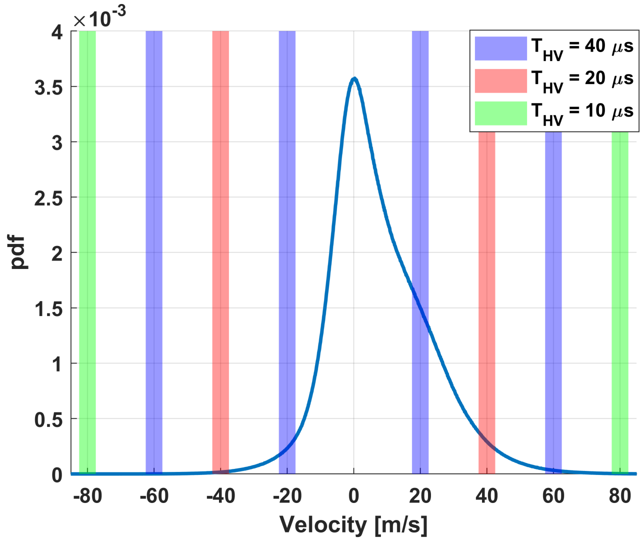

Fig. 10. Expected pdf of WIVERN LOS Doppler velocities (for azimuthal angles between 0° and 180°) with the regions where biases may occur color-coded according to three different T_{HV} selections.

There are two mechanisms through which cross-talk affects the WIVERN signal.

1) The cross-talk enhances the received power signal with the drawback of potentially altering the amount of cloud cover and water content. The optimal estimation methodology here proposed robustly recovers the co-polar reflectivity signal except for ranges where both polarization received signals are contaminated by cross-talk (here called “double ghosts”). Based on simulated WIVERN profiles reconstructed from the W-band CloudSat radar observations, such situations are typically very rare.

2) When considering Doppler velocity estimates, cross-talk signals act as an additional source of noise, being incoherent to the co-polar signals. As a result, cross-talk increases the measurement error in the line of sight Doppler velocities and thus reduces the number of precise winds. For example, in the case of $T_{HV} = 20\,\mu$s for a precision of 1 m/s, the frequency of identified wind velocities per day experienced a decrease by 11.2% under normal LDR conditions, and by 24.6% when subjected to a 10 dB LDR enhancement in comparison to the no LDR case (Table III).

The strengths of both effects depend on the H-V pair time separation, T_{HV}. A selection of T_{HV} higher than 20 μs favors more precise winds and a lower number of “double ghosts”, thus a better reconstruction of the co-polar reflectivities. However, larger T_{HV}s are detrimental because they cause aliasing in high winds and biases in the proximity of the folding velocities. As a result, the current baseline value of 20 μs seems to be a good compromise between the large (bottom) errors originated by the strong dependence on the Doppler phase noise at small T_{HV}s and those caused by the drop in correlation and unambiguous Nyquist velocity at large T_{HV}s. A thorough investigation during the commissioning phase could allow a proper selection of this parameter. In addition, the possibility of running the radar in “LDR mode” could allow for building a proper climatology on LDR and on the impact of multiple scattering on cross-talk.

APPENDIX

A. Retrieval including Z_{DR}

In the scenario where $Z_{\mathrm{DR}} \neq 0$, the previously assumed equality of $P_{\mathrm{HH}}(r) = P_{\mathrm{VV}}(r) = P_{\mathrm{co}}(r)$ is no longer applicable, leading to three unknown variables: P_{HH}, P_{VV}, and $P_{\mathrm{cx}} = P_{\mathrm{HV}} = P_{\mathrm{VH}}$ (this holds in any case because of the symmetries of phase matrix at backscattering [22]). Consequently, the system of equations presented in Eq. (1) is underdetermined. Under these circumstances, Eq. (1) and (2) provides a set of two independent equations that can be exploited to solve the problem. The received signals at the horizontal (H) and vertical (V) receivers from both polarization-diversity pairs (H-V and V-H), described by the four equations (1-2), can be solved through an iterative process to determine the values of the three unknowns at each iteration level:

$$P_{\mathrm{HH}}(i) = \begin{cases} 0, \quad i = 1, \ldots, n_{HV} \\ P_{\mathrm{H}}^{\text{H-V}}[i], \quad i = n_{HV}+1, \ldots, 2n_{HV} \\ P_{\mathrm{H}}^{\text{H-V}}[i] - P_{\mathrm{V}}^{\text{H-V}}[i-2n_{HV}], \\ \qquad i = 2n_{HV}+1, \ldots, 3n_{HV} \\ P_{\mathrm{H}}^{\text{H-V}}[i] - P_{\mathrm{V}}^{\text{H-V}}[i-2n_{HV}] + P_{\mathrm{VV}}[i-2n_{HV}], \\ \qquad i \geq 3n_{HV}+1 \end{cases}$$

$$P_{\mathrm{VV}}(i) = \begin{cases} 0, \quad i = 1, \ldots, n_{HV} \\ P_{\mathrm{V}}^{\text{V-H}}[i], \quad i = n_{HV}+1, \ldots, 2n_{HV} \\ P_{\mathrm{V}}^{\text{V-H}}[i] - P_{\mathrm{H}}^{\text{V-H}}[i-2n_{HV}], \\ \qquad i = 2n_{HV}+1, \ldots, 3n_{HV} \\ P_{\mathrm{V}}^{\text{V-H}}[i] - P_{\mathrm{H}}^{\text{V-H}}[i-2n_{HV}] + P_{\mathrm{HH}}[i-2n_{HV}], \\ \qquad i \geq 3n_{HV}+1 \end{cases}$$

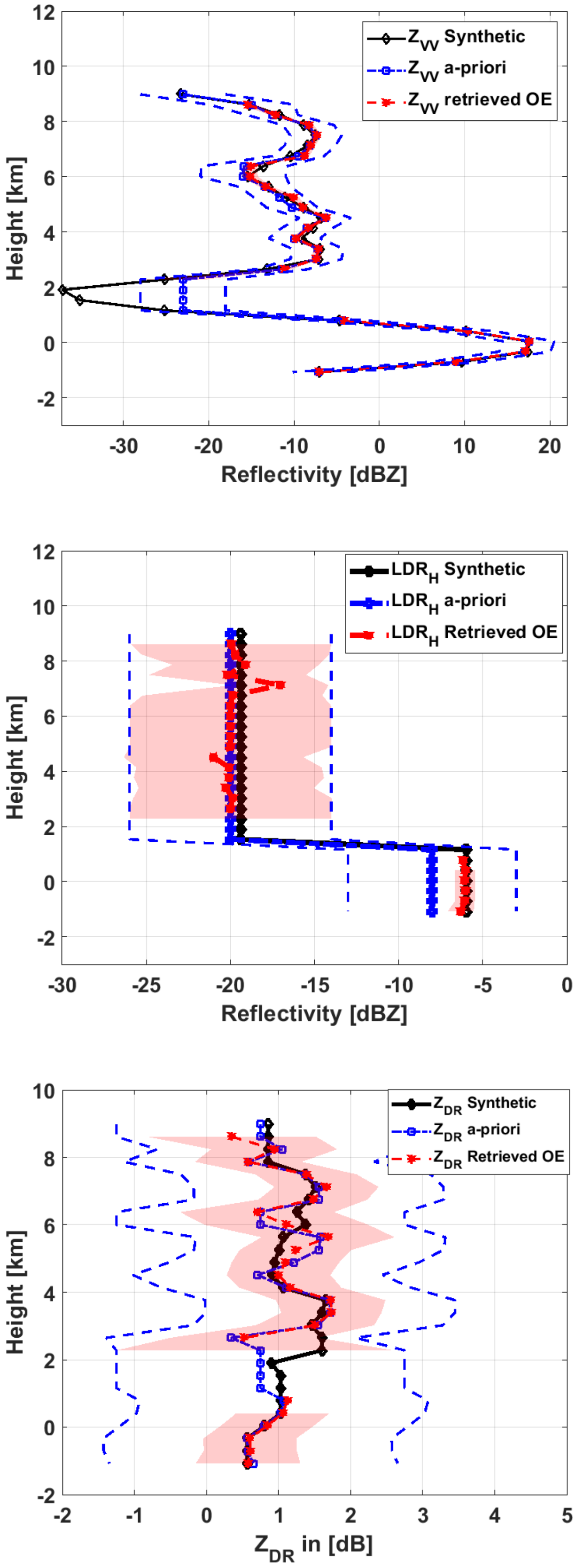

Fig. 11. Retrieved co-polar V reflectivity (top), LDR_H (middle), and Z_{DR} for the profile shown in Fig. 2. A-priori and synthetic profiles are shown in blue and black color. A 5 km averaging is considered. The error standard deviation of the OE solution is in red while the blue dashed lines represent the uncertainty on the a-priori

$$P_{\text{cx}}(i) = \begin{cases} 0, \quad i = 1,\dots,n_{HV} \\[2ex] P_{\text{H}}^{\text{V-H}}[i], \quad i = n_{HV}+1,\dots,2n_{HV} \\[2ex] P_{\text{V}}^{\text{H-V}}[i-n_{HV}] - P_{\text{V}}^{\text{V-H}}[i-n_{HV}], \\ \qquad\qquad\qquad i = 2n_{HV}+1,,\dots,3n_{HV} \\[2ex] P_{\text{V}}^{\text{H-V}}[i-n_{HV}] - P_{\text{V}}^{\text{V-H}}[i-n_{HV}] + P_{\text{cx}}[i-2n_{HV}], \\ \qquad\qquad\qquad i \geq 3n_{HV}+1 \end{cases}$$

It is important to emphasize that the current system of equations does not take into account the noise at this stage. It solely illustrates the ideal solution achieved through the iterative approach in the presence of Z_{DR}. However, the noise is subsequently incorporated into the simulated data before applying the iterative approach and utilizing the OE.

The optimal estimation components now become.

1) Unknowns: P_{VV}, $\text{LDR}_\text{H} = \frac{P_{\text{HV}}}{P_{\text{HH}}}$, $Z_{\text{DR}} = \frac{P_{\text{HH}}}{P_{\text{VV}}}$.
2) Measurements: $P_{\text{H}}^{\text{H-V}}$, $P_{\text{V}}^{\text{H-V}}$, $P_{\text{H}}^{\text{V-H}}$, $P_{\text{V}}^{\text{V-H}}$
3) Forward Model:

$$\begin{cases} P_{\text{H}}^{\text{H-V}}[i] = Z_{\text{DR}}[i]P_{\text{VV}}[i] + \text{LDR}_\text{H}[i-n_{hv}]Z_{\text{DR}}[i-n_{hv}] \\ \qquad P_{\text{VV}}[i-n_{hv}] \\[2ex] P_{\text{V}}^{\text{H-V}}[i] = P_{\text{VV}}[i] + \text{LDR}_\text{H}[i+n_{hv}]Z_{\text{DR}}[i+n_{hv}] \\ \qquad P_{\text{VV}}[i+n_{hv}] \\[2ex] P_{\text{H}}^{\text{V-H}}[i] = Z_{\text{DR}}[i]P_{\text{VV}}[i] + \text{LDR}_\text{H}[i+n_{hv}]Z_{\text{DR}}[i+n_{hv}] \\ \qquad P_{\text{VV}}[i+n_{hv}] \\[2ex] P_{\text{V}}^{\text{V-H}}[i] = P_{\text{VV}}[i] + \text{LDR}_\text{H}[i-n_{hv}]Z_{\text{DR}}[i-n_{hv}] \\ \qquad P_{\text{VV}}[i-n_{hv}] \end{cases}$$

4) Methodology for choosing the a-priori. Following the iterative solution, the present study employs the identical methodology presented in section III-B to determine the a-priori for Z_{VV} and LDR_H. Subsequently, the a-priori values of Z_{HH} and Z_{VV} are utilized in calculating the a-priori for Z_{DR}. Further, at locations where both SNR_H and SNR_V are below 3 dB, the prior values of Z_{DR} are substituted with the mean values derived from simulated data based on temperature conditions, namely, ice, melting, and rain (see Appendix B).

A demonstration of the retrieval performance using Z_{DR} applied to the profile depicted in Fig. 2 is presented in Fig. 11.

The proposed methodology for the a-priori estimation exhibits a high level of accuracy for both the co-polar Z_{VV} and Z_{DR} parameters, leveraging the a-priori knowledge of the co-polar measurements. However, the optimal estimation (OE) solution outperforms the proposed methodology, particularly in regions where the signal is close to the noise level. Conversely, the retrieval of linear depolarization ratio (LDR) is predominantly influenced by the prior assumption, with the OE approach largely adhering to the prior information and only making minor enhancements at specific locations. Notably,

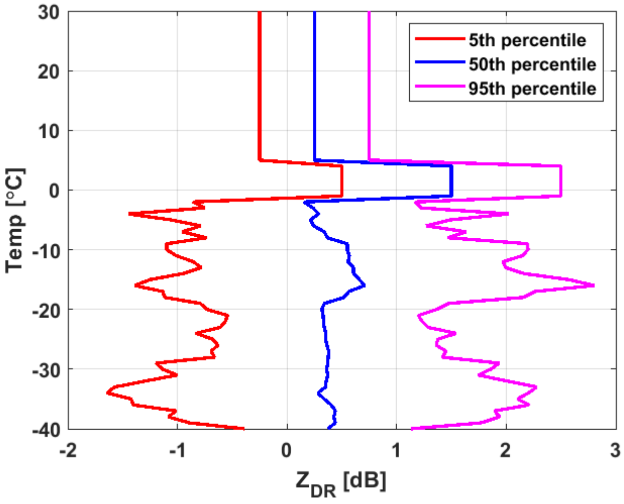

Fig. 12. Simulated Z_{DR} profiles at the 5^{th}, 50^{th}, and 95^{th} percentiles.

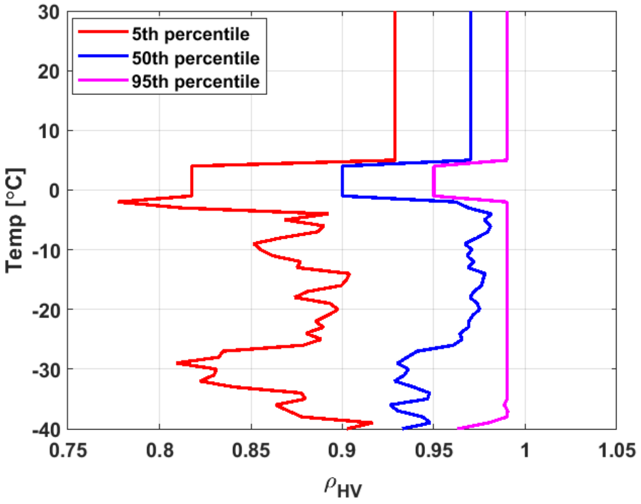

Fig. 13. Simulated ρ_{HV} profiles at the 5^{th}, 50^{th}, and 95^{th} percentiles.

the OE solution achieves significantly superior accuracy in characterizing the LDR of the surface, converging to the true LDR value.

B. Simulation of Realistic Polarimetric Variables

This section outlines the methodology employed to simulate accurate Z_{DR} profiles for the purpose of simulating the WIVERN signal when $Z_{\mathrm{DR}} \neq 0$. To achieve this, a collection of polarimetric variable measurements obtained in Colorado, USA is employed. The Z_{DR} profile illustrated in Fig. 11 serves as an example of the realistic profiles generated through this simulation process.

1) Description of W-band radar observations in Colorado: As part of the SAIL experiment (https://sail.lbl.gov), a winter campaign focusing on cloud and precipitation took place in Colorado, USA at the Rocky Mountains Biological Laboratory site (altitude: 2913 m; latitude: 38°57'37.11"N; longitude: 106°59'27.28"W) from November 2022 to June 2023. It involved extensive measurements utilizing the Leipzig University W-band cloud radar [23], at an elevation angle of 40 degrees and an in-situ newly developed snowfall camera called VISSS [24]. Additional measurements were conducted including 12-hourly radio soundings for tropospheric profiling. The dataset utilized in this study comprised profiles of atmospheric temperature (T°C), differential reflectivity (Z_{DR}), and the cross-correlation coefficient (ρ_{HV}).

2) Generation of Realistic Z_{DR} Profiles: To assess the retrieval performance under the condition where $Z_{DR} \neq 0$, it is necessary to generate realistic Z_{DR} profiles in the simulations. To accomplish this, the dataset obtained from the ice and snow measurements in Colorado and from the rain and melting layer at the Chilbolton Observatory is utilized. Three distinct regions are defined: ice ($T < -1$°C), melting layer ($-1° \leq T \leq 4$°C), and rain ($T > 4$°C). Within the ice region, Z_{DR} measurements extracted from the Colorado dataset at each temperature are utilized with a precision of 1°C. Subsequently, the mean and standard deviation of these measurements are determined. For the melting layer and rain regions, two normal distributions of Z_{DR} values are employed: $\mathcal{N}(1.5, 0.5)$ and $\mathcal{N}(0.25, 0.25)$, respectively. By randomly selecting a certain percentile from each distribution, the Z_{DR} profile at that percentile is obtained by multiplying the chosen percentile by the standard deviation and shifting it by the mean. An example showing the simulated Z_{DR} profiles for different percentiles is presented in Fig. 12.

3) Generation of Realistic ρ_{HV} Profiles: Using a similar methodology, the Colorado ice data is utilized to generate realistic profiles of ρ_{HV}. The data is categorized into the same aforementioned temperature regions. For the ice region, the ρ_{HV} measurements from the Colorado dataset are employed, with a precision of 1°C for each temperature, then the mean and standard deviation of these measurements are subsequently calculated. In the melting layer and rain regions, two normal distributions of ρ_{HV} values: $\mathcal{N}(0.9, 0.05)$ and $\mathcal{N}(0.97, 0.025)$ are employed, respectively. After, the ρ_{HV} profile at a specific percentile is generated by multiplying the selected percentile by the standard deviation and shifting by the mean. An illustrative example depicting the simulated ρ_{HV} profiles for various percentiles is provided in Fig. 13.

It's important to note that for values of ρ_{HV} exceeding 1, starting from the 95th percentile, they are capped at 0.99 in ice/rain conditions and 0.95 in melting conditions. This adjustment is crucial for maintaining realistic correlation values and preventing ρ_{HV} from exceeding 1.

4) Generation of Realistic LDR Profiles: The climatological LDR values of the hydrometeors, expressed in dB, are obtained through a reconstruction process based on both temperature and cloud type using the 2B-CLDCLASS-LIDAR classification [25]. To construct a climatology of LDR profiles with respect to temperature, data was collected during a specific field campaign at the Chilbolton observatory in June and July 2017. During this campaign, the W-band Galileo polarimetric radar was directed at a 45° elevation angle.

The resulting LDR profiles' 5^{th}, 50^{th}, and 95^{th} percentiles are illustrated in Fig. 14. Subsequently, LDR values are re-

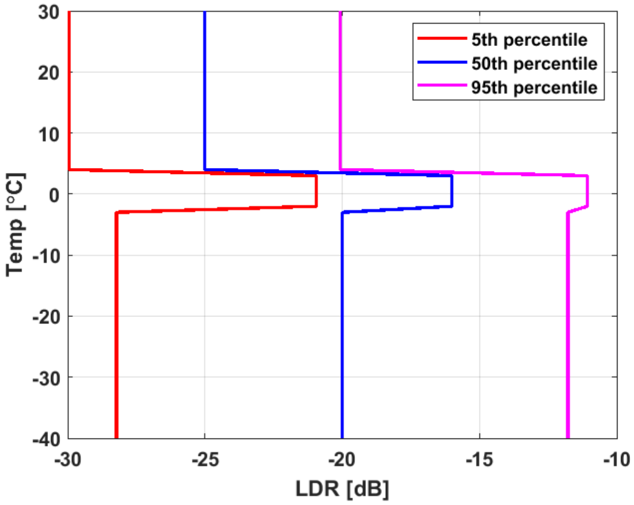

Fig. 14. Simulated LDR profiles at the 5^{th}, 50^{th}, and 95^{th} percentiles.

constructed from the climatological quantiles, assuming normal distributions with mean values and standard deviations determined based on the cloud class and temperature range (i.e., ice, melting, and rain). The LDR normal distributions at each temperature range utilize the mean and standard deviation values presented in section III-B.

ACKNOWLEDGMENTS

This research has been supported by the European Space Agency under the activities “WInd VElocity Radar Nephoscope (WIVERN) Phase 0 Science and Requirements Consolidation Study” (ESA Contract Number 4000136466/21/NL/LF) and “End-to-End Performance Simulator Activity of the WIVERN Mission” (ESA Contract Number 4000139446/22/NL/SD). The research campaign in Colorado was supported by the Deutsche Forschungsgemeinschaft (project no. 408008112). Thanks also to the Rocky Mountain Biological Laboratory in Crested Butte, Colorado, USA, and the Atmospheric Radiation Measurement (ARM) user facility of the U.S. Department of Energy (DOE) for research support within the frame of the SAIL experiment. This research used the Mafalda cluster at Politecnico di Torino.

REFERENCES

[1] A. J. Illingworth, A. Battaglia, J. Bradford, M. Forsythe, P. Joe, P. Kollias, K. Lean, M. Lori, J.-F. Mahfouf, S. Melo, R. Midthassel, Y. Munro, J. Nicol, R. Potthast, M. Rennie, T. H. M. Stein, S. Tanelli, F. Tridon, C. J. Walden, and M. Wolde, “WIVERN: A New Satellite Concept to Provide Global In-Cloud Winds, Precipitation, and Cloud Properties,” vol. 99, no. 8, pp. 1669–1687, 2018. [Online]. Available: https://doi.org/10.1175/BAMS-D-16-0047.1

[2] A. Battaglia, P. Martire, E. Caubet, L. Phalippou, F. Stesina, P. Kollias, and A. Illingworth, “End to end simulator for the wivern w-band doppler conically scanning spaceborne radar,” vol. 2021, pp. 1–31, 2022. [Online]. Available: https://amt.copernicus.org/preprints/amt-2021-342/

[3] R. J. Doviak and D. S. Zrnić, *Doppler Radar and Weather Observations*. Academic Press, 1993.

[4] A. L. Pazmany, J. C. Galloway, J. B. Mead, I. Popstefanija, R. E. McIntosh, and H. W. Bluestein, “Polarization Diversity Pulse-Pair Technique for Millimeter-WaveDoppler Radar Measurements of Severe Storm Features,” vol. 16, no. 12, pp. 1900–1911, 1999. [Online]. Available: https://doi.org/10.1175/1520-0426(1999)016⟨1900:PDPPTF⟩2.0.CO;2

[5] A. Battaglia, S. Tanelli, and P. Kollias, “Polarization Diversity for Millimeter Spaceborne Doppler Radars: An Answer for Observing Deep Convection?” vol. 30, no. 12, pp. 2768–2787, 2013. [Online]. Available: https://doi.org/10.1175/JTECH-D-13-00085.1

[6] S. Tanelli, S. L. Durden, E. Im, K. S. Pak, D. G. Reinke, P. Partain, J. M. Haynes, and R. T. Marchand, “CloudSat’s Cloud Profiling Radar After Two Years in Orbit: Performance, Calibration, and Processing,” vol. 46, no. 11, pp. 3560–3573, Nov 2008.

[7] A. J. Illingworth, H. W. Barker, A. Beljaars, M. Ceccaldi, H. Chepfer, N. Clerbaux, J. Cole, J. Delanoë, C. Domenech, D. P. Donovan, S. Fukuda, M. Hirakata, R. J. Hogan, A. Huenerbein, P. Kollias, T. Kubota, T. Nakajima, T. Y. Nakajima, T. Nishizawa, Y. Ohno, H. Okamoto, R. Oki, K. Sato, M. Satoh, M. W. Shephard, A. Velázquez-Blázquez, U. Wandinger, T. Wehr, and G.-J. van Zadelhoff, “The EarthCARE Satellite: The Next Step Forward in Global Measurements of Clouds, Aerosols, Precipitation, and Radiation,” vol. 96, no. 8, pp. 1311–1332, 2015. [Online]. Available: https://doi.org/10.1175/BAMS-D-12-00227.1

[8] P. Kollias, B. Puidgomènech Treserras, A. Battaglia, P. Borque, and A. Tatarevic, “Processing reflectivity and doppler velocity from earthcare’s cloud profiling radar: the c-fmr, c-cd and c-apc products,” *EGUsphere*, vol. 2022, pp. 1–25, 2022. [Online]. Available: https://egusphere.copernicus.org/preprints/egusphere-2022-1284/

[9] K. Mroz, B. P. Treserras, A. Battaglia, P. Kollias, A. Tatarevic, and F. Tridon, “Cloud and precipitation microphysical retrievals from the earthcare cloud profiling radar: the c-cld product,” *EGUsphere*, vol. 2023, pp. 1–33, 2023. [Online]. Available: https://egusphere.copernicus.org/preprints/egusphere-2023-56/

[10] M. Wolde, A. Battaglia, C. Nguyen, A. L. Pazmany, and A. Illingworth, “Implementation of polarization diversity pulse-pair technique using airborne w-band radar,” vol. 12, no. 1, pp. 253–269, 2019. [Online]. Available: https://www.atmos-meas-tech.net/12/253/2019/

[11] V. N. Bringi and V. Chandrasekar, *Polarimetric Doppler Weather Radar, Principles and applications*. Cambridge University Press, 2001, pp 266.

[12] A. Battaglia, M. O. Ajewole, and C. Simmer, “Evaluation of radar multiple scattering effects in Cloudsat configuration,” *ACP*, vol. 7, no. 7, pp. 1719–1730, 2007. [Online]. Available: https://www.atmos-chem-phys.net/7/1719/2007/

[13] A. Battaglia, S. Tanelli, S. Kobayashi, D. Zrnic, R. J. Hogan, and C. Simmer, “Multiple-scattering in radar systems: A review,” vol. 111, no. 6, pp. 917 – 947, 2010. [Online]. Available: http://www.sciencedirect.com/science/article/pii/S0022407309003677

[14] A. Pazmany, R. McIntosh, R. Kelly, and G. Vali, “An airborne 95 GHz dual-polarized radar for cloud studies,” vol. 32, no. 4, pp. 731–739, 1994, doi:10.1109/36.298002.

[15] A. Myagkov, S. Kneifel, and T. Rose, “Evaluation of the reflectivity calibration of w-band radars based on observations in rain,” vol. 13, no. 11, pp. 5799–5825, 2020. [Online]. Available: https://amt.copernicus.org/articles/13/5799/2020/

[16] M. I. Mishchenko, J. W. Hovenier, and L. D. Travis, Eds., *Light Scattering by Nonspherical Particles*. Academic Press, 2000.

[17] A. Battaglia, R. Dhillon, and A. Illingworth, “Doppler W-band polarization diversity space-borne radar simulator for wind studies,” vol. 11, no. 11, pp. 5965–5979, 2018. [Online]. Available: https://www.atmos-meas-tech.net/11/5965/2018/

[18] F. Tridon, A. Battaglia, A. Rizik, F. Scarsi, and A. Illingworth, “Filling the gap of wind observations inside tropical cyclones,” *Earth and Space Science*, 2023.

[19] A. Battaglia, M. Wolde, L. P. D’Adderio, C. Nguyen, F. Fois, A. Illingworth, and R. Midthassel, “Characterization of Surface Radar Cross Sections at W-Band at Moderate Incidence Angles,” vol. 55, no. 7, pp. 3846–3859, 2017, 10.1109/TGRS.2017.2682423.

[20] C. D. Rodgers, *Inverse methods for atmospheric sounding: theory and practice*, ser. Series on atmospheric, oceanic, and planetary physics. Singapore: World Scientific, 2000, no. 2.

[21] S. Tanelli, E. Im, L. Facheris, and E. A. Smith, “DFT-based spectral moment estimators for spaceborne Doppler precipitation radar,” in *Proc. of Symp. on Rem. Sens. of the Atmosphere, Environment and Space (SPIE 4894-50)*, Hangzhou (RPC), 2002.

[22] M. I. Mishchenko, J. W. Hovenier, and L. D. Travis, Eds., *Light Scattering by Nonspherical Particles: Theory, Measurements, and Applications*. San Diego: Academic Press, 2000.

[23] N. Küchler, S. Kneifel, U. Löhnert, P. Kollias, H. Czekala, and T. Rose, "A w-band radar–radiometer system for accurate and continuous monitoring of clouds and precipitation," *Journal of Atmospheric and Oceanic Technology*, vol. 34, no. 11, pp. 2375 – 2392, 2017. [Online]. Available: https://journals.ametsoc.org/view/journals/atot/34/11/jtech-d-17-0019.1.xml

[24] M. Maahn, D. Moisseev, I. Steinke, N. Maherndl, and M. D. Shupe, "Introducing the video in situ snowfall sensor (visss)," *EGUsphere*, vol. 2023, pp. 1–27, 2023. [Online]. Available: https://egusphere.copernicus.org/preprints/2023/egusphere-2023-655/

[25] K. Sassen, Z. Wang, and D. Liu, "The global distribution of cirrus clouds from CloudSat/CALIPSO measurements," vol. 113, no. D00A12, 2008, doi:10.1029/2008JD009972.

Ali Rizik holds a diverse academic background, culminating in a Ph.D. in Science and Technology for Electronic and Telecommunication Engineering from the Department of Naval, Electrical, Electronic, and Telecommunications Engineering (DITEN) at the University of Genoa, Italy, in 2021. His journey began with a graduation from the Faculty of Science at the Lebanese University in 2016, where he delved into signal, telecom, image, and speech processing through his thesis. His international exposure includes an internship at ULCO University, France, from April to August 2016, which further enriched his academic and professional experience. Currently, he occupies a postdoctoral position at DIATI at the Politecnico di Torino, Turin, Italy, contributing to the WIVERN spaceborne Doppler radar project. His research interests encompass a broad spectrum, with a primary focus on machine learning applications, radar signal processing, radar target identification for security applications, and the application of radars in meteorology. His research interests also include space-borne remote sensing and atmospheric convection science.

Alessandro Battaglia graduated at the University of Padova, Italy, with a thesis in Particle Physics and received the Ph.D. degree in Physics at the University of Ferrara, Italy. He is experienced in microwave remote sensing of clouds and precipitation with a specific interest in space-borne radars. Currently, he has a joint appointment as an Associate Professor in the Department of Physics at the University of Leicester, Leicester, UK, and at DIATI at Politecnico di Torino, Turin, Italy. He has extensive experience in active and passive microwave modeling, he has developed radar forward modeling capable of simulating Doppler space-borne radars, he has worked on polarization diversity, and developed retrieval algorithms for multi-frequency observations. He is a member of the NASA Precipitation Measuring Mission Science Team and of the INCUS Team, a member of the ESA MAG of EarthCARE and WIVERN, and an author or co-author of more than 100 peer-reviewed journal papers.

Frederic Tridon completed his PhD in radar meteorology in 2011 at the Laboratoire de Météorologie Physique at Blaise Pascal University in Clermont-Ferrand (France). As a PostDoc, he worked successively at the Department of Physics of the University of Leicester (UK), at the Institute of Geophysics and Meteorology of the University of Cologne (Germany), and is now at DIATI at Politecnico di Torino, Turin (Italy). His research focuses on the characterization of the microphysical processes of cloud and precipitation for a better understanding of their role in the earth's radiation budget and water cycle. In particular, he has extensive experience in the retrieval of liquid and solid precipitation properties, combining multiple-frequency radars, from ground-based, airborne, and spaceborne platforms.

Filippo Emilio Scarsi received his M.S. degree in aerospace engineering from the Polytechnic of Turin, Italy. He is now pursuing a Ph.D. degree, with a focus on the INCUS mission, at the Polytechnic of Turin and at IUSS Pavia, Italy. His research interests include space-borne remote sensing and atmospheric convection science.

Anton Kötsche has received a bachelor's and master's degree in meteorology at the University of Leipzig, Germany in 2020 and 2022 and is currently a PhD at the University of Leipzig. His research centers on the microphysical process understanding of snow formation in orographic terrain using polarimetric cloud radar data.

Heike Kalesse-Los has received a PhD degree in Meteorology at the Johannes Gutenberg University in Mainz, Germany in 2010 and was a PostDoc at McGill University in Montreal, Canada from 2011-2014. Currently, she is a tenure-track professor of Arctic Climate Change and Remote Sensing of the Atmosphere at Leipzig University, Germany. Her research centers on microphysical process understanding of clouds and precipitation formation around the globe with a focus on Arctic mixed-phase clouds, Southern Ocean clouds, and trade-wind clouds. In her work, she combines synergistic profiling of the atmosphere with active and passive remote sensing instruments with machine-learning methods to e.g. exploit cloud radar Doppler spectra information content for liquid detection and riming occurrence. Recently, she has also become interested in using atmospheric remote sensing observations for novel deployments, e.g. in the field of interactions between climate change and biodiversity change research.

Maximilian Maahn has received the M.S. degree in meteorology from the University of Bonn, Germany, in 2010 and the Ph.D. degree in meteorology from the University of Cologne, Germany, in 2015. He was a research scientist at the University of Cologne from 2011 to 2016, after which he moved to the Cooperative Institute for Research in Environmental Sciences (CIRES) of the NOAA Earth System Research Laboratories and the University of Colorado Boulder from 2016 to 2020. Since 2020, he leads the drOPS (clouD and pRecipitation Observations for Process Studies) group at Leipzig University. His main research interests include the improvement of remote sensing and in situ observations of clouds and precipitation. He is currently developing a novel in situ sensor for snowfall. Dr. Maahn is a member of the American Meteorological Society and the German Meteorological Society. He is an associate editor of the journal Atmospheric Measurement Techniques.

Anthony Illingworth Prof. Anthony Illingworth joined the Department of Meteorology at Reading in 1993. For over 30 years he has worked with the large 25 m radar antenna at Chilbolton, Hampshire developing methods for improved estimates of rainfall. Since 2000 he has also been involved in the development of spaceborne missions for observing cloud properties on a global scale. He has been the lead European scientist on the EarthCARE mission, a joint European/Japanese satellite due to be launched in 2024. The Doppler radar and advanced lidar on this satellite will provide global profiles of clouds, aerosol, precipitation, and radiation to better understand the earth's radiation balance and improve weather forecasts. He now chairs the WIVERN MAG.